Title

Quantitative Measurements of the Temperature-Dependent Microscopic and Macroscopic Dynamics of a Molecular Dopant in a Conjugated Polymer

Permalink
https://escholarship.org/uc/item/2394q688

Journal
Macromolecules, 50(14)

ISSN
0024-9297

Authors
Li, Jun
Koshnick, Correy
Diallo, Souleymane O
et al.

Publication Date
2017-07-25

DOI
10.1021/acs.macromol.7b00672

Peer reviewed

Macromolecules
Article
pubs.acs.org/Macromolecules

Quantitative Measurements of the Temperature-Dependent Microscopic and Macroscopic Dynamics of a Molecular Dopant in a Conjugated Polymer

Jun Li,[†] Correy Koshnick,[‡] Souleymane O. Diallo,[∥] Sophia Ackling,[#] David M. Huang,[#] Ian E. Jacobs,[‡] Thomas Harrelson,[†] Kunlun Hong,[⊥] Guangwu Zhang,[§] Joseph Beckett,[§] Mark Mascal,[§] and Adam J. Moulé*,[†]

[†]Department of Chemical Engineering, [‡]Department of Materials Science and Engineering, and [§]Department of Chemistry, University of California, Davis, Davis, California 95616, United States

[∥]Neutron Scattering Science Division and [⊥]Center for Nanophase Materials Sciences, Oak Ridge National Laboratory, Oak Ridge, Tennessee 37831, United States

[#]Department of Chemistry, School of Physical Sciences, The University of Adelaide, Adelaide, SA 5005, Australia

Supporting Information

ABSTRACT: Understanding the nature of dopant dynamics in the solid state is critical for improving the longevity and stability of organic electronic devices and for optimizing the doping-induced solubility control (DISC) patterning method. In this work, we use quasi-elastic neutron scattering (QENS) and fluorescence quenching techniques to develop a comprehensive picture of both the microscopic and macroscopic dynamics of the soluble p-type molecular dopant tetrafluoromethyloxycarbonyltricyanoquinodimethane (F4MCTCNQ) in the conductive polymer poly(3-hexylthiophene-2,5-diyl) (P3HT). Specifically, fast dynamics (ps−ns) of the dopant, such as the methyl and the methoxycarbonyl group rotations, are observed in QENS experiments. From confocal fluorescence microscope experiments, longer-range/slower dopant diffusion (ms−days) is captured. However, in order to fit these data, it is necessary to incorporate a Langmuir isotherm equilibrium between the neutral and ionized dopant molecules. Ionized F4MCTCNQ is strongly favored by the equilibrium, but it diffuses 3 orders of magnitude slower than neutral species. Moreover, the macroscopic diffusion is found to depend mostly on the minority concentration of neutral dopant molecules in the film. Finally, the global diffusion coefficient of the monoester-substituted dopant F4MCTCNQ is shown to be more than 1 order of magnitude smaller than that of the widely used dopant F4TCNQ.

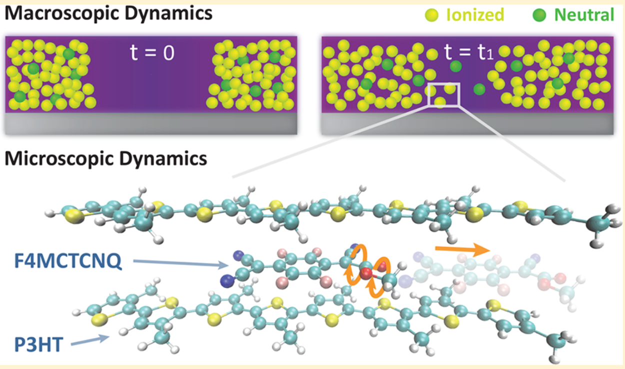

■ INTRODUCTION

The successful development of organic electronic devices, such as organic photovoltaics (OPVs),[1,2] organic light-emitting diodes (OLEDs),[3,4] and organic field-effect transistors (OFETs),[5,6] is largely attributable to the tunability of their electrical properties. Like inorganic semiconductors, organic semiconductors (OSCs) can be doped to facilitate increased charge transport[7,8] as well as decreased injection or extraction barriers via changes in the Fermi energy.[9] However, the undesired diffusion of dopants in organic electronic architectures has been known to cause serious stability and longevity issues.[10−12] Controlling dopant diffusion is also an important aspect of doping-induced solubility control (DISC), a new patterning method recently developed which allows the solubility of a conductive polymer to be switched on and off by doping and dedoping, respectively.[13−15] It has also been demonstrated that DISC is capable of using both vapor and solution processes to achieve micrometer and submicrometer resolution, respectively, in a method that is compatible with roll-to-roll solution processing.[13,16] For DISC patterning, the lateral diffusion of the dopant limits the ultimate resolution of the pattern. Therefore, for both the stability of completed organic devices and for fabrication of these devices using solution compatible methods, understanding the dynamics of the dopants is extremely important to further application development.

The measurement of small molecular dopant diffusion is particularly challenging because dopants are present in trace quantities and composed of the same light elements (C, H, O, N, S) as the host OSCs. Most of these studies so far have

Received: March 30, 2017
Revised: May 31, 2017

DOI: 10.1021/acs.macromol.7b00672

focused on the diffusion of dopants from one layer to another in a vertical layer stack. These samples are prepared by either vacuum evaporating or laminating doped and undoped layers of materials. Secondary ion mass spectrometry (SIMS) is by far the most commonly used technique for diffusion studies due to its high spatial and depth resolution in differentiating molecules. A recent study shows that SIMS can be utilized to monitor the diffusion of 2,3,5,6-tetrafluoro-7,7,8,8-tetracyanoquinodimethane (F4TCNQ), which is a widely used p-type molecular dopant, in the hole transport layer of OLEDs.[17] The SIMS signal from the fluorine atoms gives a unique isotopic label. Similar work using SIMS was also performed more recently on the diffusion of the soluble p-dopant molybdenum tris[1-(methoxycarbonyl)-2-(trifluoromethyl)-ethane-1,2-dithiolene] (Mo(tfd-$CO_2Me)_3$) into polymer and polymer blend films using the Mo label.[18] Likewise, excellent work was conducted by Treat et al. where the diffusion of phenyl-C_{61}-butyric acid methyl ester (PCBM) in poly(3-hexylthiophene-2,5-diyl) (P3HT) was quantified using SIMS and a deuterium-labeled PCBM (*d*-PCBM).[19] The same group also quantified the lateral diffusion of *d*-PCBM in P3HT using dynamic SIMS, yielding a one-dimensional diffusion coefficient using Fick's second law.[20] However, SIMS is a destructive technique, and additional etching steps are needed. In addition, a unique atom or isotopic labeling is required in order to use SIMS. Other measurement techniques, such as X-ray photoelectron spectroscopy (XPS), ultraviolet photoelectron spectroscopy (UPS), neutron/X-ray/visible light scattering, and photoluminescence, have also been used to measure the diffusion of dopants in layered samples.[21−29] Most of these studies reported whether dopants diffused beyond their original layer and at which temperature threshold. Although some were able to quantify dopant concentration at an interface or surface, only one study was able to measure diffusion as a function of distance and time. Thus, Fischer et al. quantified the temperature dependence of the diffusion coefficient in a vertical geometry using a time-resolved optical technique.[24] Finally, a series of articles have reported the observation of dopant diffusion (or lack thereof) by creating bi- or trilayers and subsequently measuring changes in the electronic properties of layer stack.[30−34] For these electronic measurements, the movement of dopants is inferred but cannot be quantified.

Previous studies have shown that dopant molecules can diffuse in a small molecule or polymer OSC host. It is known that larger dopant molecules diffuse more slowly but also have been shown to disturb the packing of the OSC and thereby to increase disorder in the local density of states.[35] Very few studies have quantified the diffusion rate of dopants. It has been assumed that the onset of diffusion occurs as a result of heating to above the glass transition temperature (T_g) of host OSC. However, one study showed that F4TCNQ diffuses at room temperature in P3HT[23] and another showed that PCBM diffuses into P3HT at 50 °C, which is below the T_g of P3HT.[19] To the best of our knowledge, no molecular level studies have looked into the mechanism for dopant binding or investigated how the properties of the host material affect the onset of dopant diffusion.

In this article, we investigate the temperature-dependent microscopic and macroscopic dynamics of the soluble p-type molecular dopant tetrafluoromethyloxycarbonyltricyanoquinodimethane (F4MCTCNQ) in P3HT. F4MCTCNQ is chosen due to its superior solubility/miscibility and thereby increased doping efficiency compared with F4TCNQ.[36] The chemical structures of the materials investigated in this paper are shown in Figure 1. F4MCTCNQ was also chosen because its methyl group carries three identical protons that can be used as a unique isotopic label in neutron scattering experiments. Quasi-elastic neutron scattering (QENS) is a well-established nondestructive technique to probe dynamic processes in soft matter.[37] In the first part of this article, we use QENS to measure the dynamics of F4MCTCNQ at the molecular scale in a sample of fully deuterated P3HT (*d*-P3HT). The protons on the F4MCTCNQ are the only hydrogen sites in the system, and ^{1}H has a much larger inelastic scattering cross section than any other isotope in the sample, allowing us to track the temperature-dependent motions of the dopant molecule only. The diffusion rate and jump distance for various microscopic motions are measured, and the motions are assigned with the aid of density functional theory (DFT) calculations. In the second part of the article, we use confocal fluorescence spectroscopy to spatially and temporally track the F4MCTCNQ concentration in patterned P3HT films, which allows us to quantify the macroscopic diffusion of the dopant. We show that macroscopic diffusion is principally dependent on the minority concentration of neutral dopant molecules in the film. This multiscale investigation gives an unprecedented mechanistic insight into dopant diffusion in OSCs.

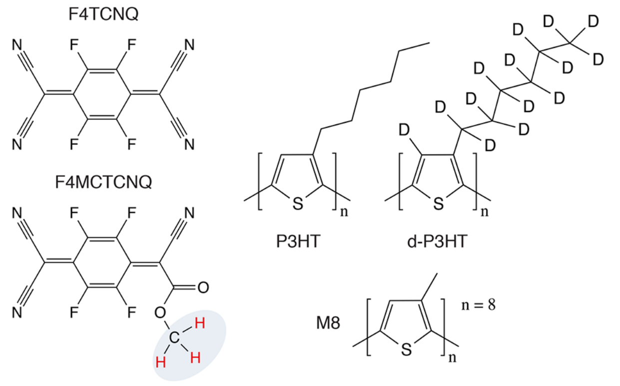

Figure 1. Chemical structures of F4TCNQ, F4MCTCNQ, P3HT, *d*-P3HT, and the simplified P3HT analogue (M8) investigated in this work.

EXPERIMENTAL SECTION

Materials. P3HT (regioregular >98%, M_n = 54−75 kDa), chlorobenzene, deuterated chlorobenzene, and molybdenum oxide (MoO_3) were purchased from Sigma-Aldrich. *d*-P3HT (regioregular >97%) and F4MCTCNQ were synthesized using the methods reported in the literature.[36,38] All chemicals were used as received unless otherwise indicated. PELCO TEM grids (1GN400, nickel) were purchased from Ted Pella, Inc.

Sample Preparation and Measurements. *Neutron Scattering.* To prepare the blend sample for QENS measurements, solutions of F4MCTCNQ and *d*-P3HT in deuterated chlorobenzene were first mixed to achieve a 17% mole fraction of dopant to polymer. The blend solution was then drop-cast onto a clean glass slide. The sample was placed into a vacuum chamber to completely evaporate the solvent. The resulting blend layer was scraped from the glass slide using a clean razor blade. Both blend and neat samples were ground to a power using a mortar and pestle for 15 min and then weighed prior to being loaded into a 0.5 mm thick flat aluminum container for further analysis.

QENS measurements were performed on the backscattering spectrometer called BASIS at the Spallation Neutron Source (SNS) at Oak Ridge National Laboratory (ORNL) with an energy resolution of 3.5 μeV (full width at half-maximum, fwhm), a dynamic range of ±170 μeV, and a scattering wavevector Q range from 0.3 to 2.0 $Å^{-1}$.[39] The elastic scans were obtained from 50 to 375 K at a heating rate of 1 K/min, and the high statistical QENS spectra were recorded at 273, 323, and 373 K. The spectra collected at 50 K were used as the instrument resolution function, and all the data were corrected for detector efficiency using a vanadium standard.

Confocal Spectroscopy. To prepare samples for the macroscopic diffusion measurements, P3HT films of ∼50 nm thickness were first obtained by spin-coating 10 mg/mL P3HT from a chlorobenzene solution onto clean glass substrates (cleaned in ultrasonic baths of acetone, 5% Mucasol detergent, and deionized water, followed by drying with nitrogen and exposure to UV/ozone for 30 min). A TEM grid (400 mesh; hole width 38 μm; bar width 26 μm) was subsequently placed onto the P3HT film using Kapton tape. Next, a 2.2 nm F4MCTCNQ layer was deposited onto the P3HT film using an MBraun thermal evaporator at a deposition rate ∼0.1 Å/s at ∼80 °C, followed by the deposition of 50 nm MoO_3 and 100 nm Ag, also via evaporation. Prior to deposition, the evaporation chamber was pumped down to a pressure of 5×10^{-6} mbar. Finally, the samples were encapsulated in an epoxy resin under a glass coverslip to ensure complete isolation from O_2 and H_2O. All fabrication steps were performed inside a nitrogen glovebox.

The confocal fluorescence (FL) microscope images were obtained on a Zeiss LSM 700 microscope equipped with a 488 nm laser and a 20× objective with 0.6 numerical aperture. These confocal FL images (16-bit, 2048 × 2048 pixels of 320 μm size) were captured at the same position before and after annealing at various temperatures (298, 323, 348, and 373 K) for various time steps by tracking the position of the marked center of the TEM grid.

Data Analysis. *Neutron Data Analysis.* For the data analysis, the dynamic range was from −120 to +120 μeV. The relevant momentum transfer range in this study was limited to 0.5−1.3 $Å^{-1}$ given the signal-to-noise ratio, the flat-plate geometrical limit, and the uncertainty of the background subtraction. DAVE software was used for data reduction and analysis.[40] The neat *d*-P3HT spectra were subtracted from the F4MCTCNQ doped *d*-P3HT spectra for all the QENS data analyses to ensure that the signal from F4MCTCNQ could be isolated.

In general, the experimentally observed scattering intensity $S_{exp}(Q,\omega)$ at each Q and temperature is expressed as the convolution of the model function $S_{model}(Q,\omega)$ and the resolution function $R(Q,\omega)$, plus a linear background term $B(Q,\omega)$:[41]

$$S_{exp}(Q, \omega) = S_{model}(Q, \omega) \otimes R(Q, \omega) + B(Q, \omega) \quad (1)$$

Here, the model function can be separated into an elastic component (a delta function $\delta(\omega)$) and a quasi-elastic contribution $S_{qe}(Q,\omega)$:

$$S_{model}(Q, \omega) = \mathrm{DWF}(Q)[A_0(Q)\delta(\omega) + (1 - A_0(Q))S_{qe}(Q, \omega)] \quad (2)$$

where DWF(Q) is the Debye−Waller factor due to the vibrational motions and $A_0(Q)$ is the elastic incoherent structure factor (EISF) defined as the fraction of elastic scattering. The proposed expression for $S_{qe}(Q,\omega)$ will be addressed in detail in the Results and Discussion section.

Macroscopic Diffusion Model. The location of dopants within the P3HT films was determined by measuring the fluorescence intensity of P3HT as a function of position using a confocal microscope and 488 nm excitation. The concentration of the dopants was determined by comparing to a calibration curve of fluorescence intensity in P3HT as a function of known doping density and assuming that there is no vertical doping gradient (reasonable for diffusion over μm in an ∼50 nm thick film). A two-dimensional two-species (2D2S) diffusion model was developed to fit the 2D doping profiles. The two diffusing species in this model were treated using a Langmuir isotherm equilibrium,[42] which was precedented for P3HT/dopants in a previous publication.[14] In terms of detailed fits, the 2D concentration profile images were initially evolved based on the above-mentioned diffusion model and then evolved using a stepwise solution to Fick's second law. The finite-difference method using a forward time-centered difference scheme was used to evolve the model in time. After each profile was evolved one time step into the future, the ratio of doped to undoped F4MCTCNQ was re-equilibrated as a function of position and concentration using the Langmuir equilibrium. In this rapid equilibration, it is assumed that the reaction rate between two species is much faster than the rate of diffusion. In doing so, the diffusion coefficients for the two species could be treated as fitting parameters and optimized based on minimization of the sum of squared residuals.

Computational Method. An eight-unit methyl-substituted oligothiophene (M8) oligomer was used as a model for a P3HT chain. The oligomer was optimized in isolation at the B3LYP/6-31G* level of theory with Grimme D2 dispersion correction (B3LYP-D).[43,44] In the absence of a dielectric medium, two of these optimized oligomers were then placed at two distinct intermolecular separations (6.30 and 6.96 Å), and a F4MCTCNQ molecule was placed midway between and parallel with the two M8 chains. These two intermolecular separations were chosen based on the optimized M8/F4TCNQ system.[45] The chains were fixed while the F4MCTCNQ was free to relax during a geometry optimization at the B3LYP-D/6-31G* level. A dielectric constant of 3.0 was used as it has been shown to be appropriate for organic semiconductors.[46−49] The lowest energy geometry was found to be that with the ring of the F4MCTCNQ stacked over the central inter-thiophene bond and the ester methyl group on the opposite side of the M8 chain methyl groups. The two separations were chosen as twice the distance between a single M8 chain and F4MCTCNQ molecule from an unconstrained geometry optimization using B3LYP with and without the dispersion correction, respectively. The two M8 oligomers were constrained in the optimization of the full system to prevent unphysical wrapping of the chains around the F4MCTCNQ molecule. These two intermolecular separations were used to give an estimate of possible variations in the energy barriers to rotation and translation due to variations in the interchain separation. Since it was found that introducing solvent into this system does not affect the intermolecular separation, the values from systems without the dielectric continuum were used.

To calculate the potential energy barrier for F4MCTCNQ translation along the polymer backbone axis, atoms in the M8 chains were fixed while the F4MCTCNQ was free to relax in a set of optimizations, subject to a position constraint applied by fixing one atom in the F4MCTCNQ. This set of translation optimizations spanned up to two thiophene units.

To calculate the potential energy barrier for F4MCTCNQ methyl rotation between the two M8 chains for both interchain separations, all atoms in the system excluding the ester methyl hydrogens were fixed, and these hydrogens were free to relax in a set of optimizations subject to dihedral angle constraints spanning 120°. In addition, calculations on an isolated F4MCTCNQ molecule were performed, in which no atom positions were fixed. Solvent was used in these calculations. Similar calculations were performed to calculate the barrier for the F4CTCNQ methoxycarbonyl rotation, but only for the isolated molecule and for the molecule between M8 chains separated by 6.96 Å.

■ RESULTS AND DISCUSSION

Part One: Microscopic Dynamics of Molecular Dopant. *Elastic Incoherent Neutron Scattering.* The microscopic dynamics of the F4MCTCNQ molecule were investigated using neutron scattering. To determine the temperature range at which the dynamic transitions of protons take place and become observable on BASIS, facile elastic incoherent neutron scattering experiments were performed first. The elastic scans of the F4MCTCNQ doped *d*-P3HT blend measured from 50 to 375 K at various Q values are shown in Figure 2a. Generally, the elastic intensity decreases monotonically with temperature due to Debye−Waller thermal factors, while any observed dynamics of the species lead to further reduction of the elastic intensity.[50] The divergence from f2

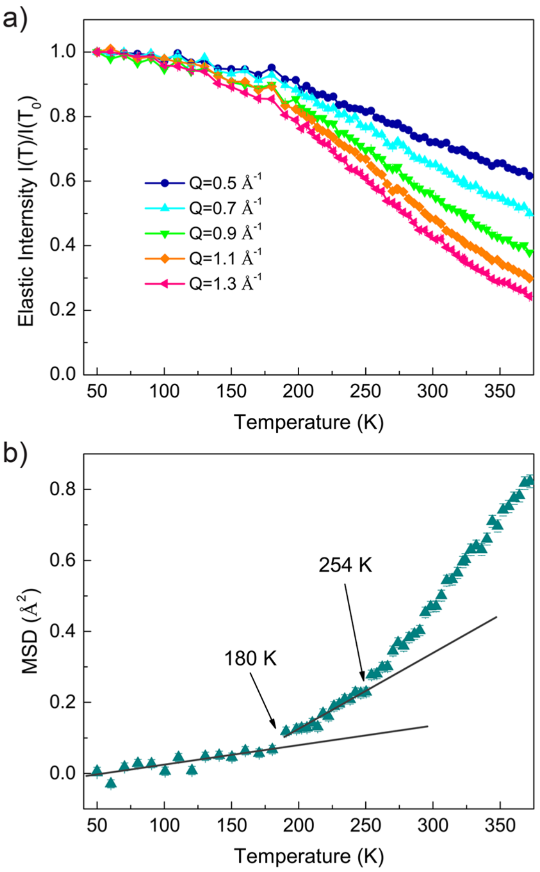

Figure 2. (a) Normalized elastic scattering intensity at various Q and (b) mean-square displacement (MSD) as a function of temperature for the F4MCTCNQ doped *d*-P3HT blend.

the monotonic decrease as a function of increasing temperature indicates the onset of molecular motions for hydrogen sites in this system.

To enhance conceptual understanding of this dynamic process, the temperature dependence of the proton mean-square displacement (MSD) determined from analysis of the elastic scans (Supporting Information section 2) was investigated. From Figure 2b, the MSD values do not vary much at temperatures below 180 K because only some local vibrations are expected to occur at such low temperatures. As the temperature increases, two deviations (changes in slope) are observed: one at about 180 K and another at 254 K. We attribute the first deviation at ~180 K to the activation of methyl group rotations, which are well-known to occur between 100 and 220 K.[51−53] On the other hand, the second deviation at ~254 K implies that another dynamic transition takes place in this temperature region. This transition could not be assigned unambiguously without further analysis.

Quasi-Elastic Neutron Scattering (QENS). To assign the dynamic transition starting at ~254 K, the high statistical scattering data were collected at temperatures above 254 K in order to capture this transition, and detailed analyses were performed. As mentioned earlier, neat *d*-P3HT spectra were also collected at the corresponding temperatures and subtracted from the spectra of the doped samples (Supporting Information section 3). In this manner, any changes of the scattering spectra explicitly result from the dynamics of the hydrogen sites in the dopants.

Representative neutron scattering spectra of subtracted doped *d*-P3HT at $Q = 0.9$ Å $^{-1}$ at three temperatures (273, 323, and 373 K) are shown in Figure 3. The experimental resolution functions collected at 50 K are also plotted. In general, the spectra can be described as a superposition of two contributions: (1) a Gaussian distribution corresponding to the elastic portion and (2) a broad shoulder in the quasielastic region. The broadening of the quasi-elastic components with increasing temperature seen from Figure 3 (it is more obvious in their normalized spectra) provides clear evidence of the occurrence of dynamic processes, which is consistent with the MSD results from elastic scans. Similar broadening features are also observed at other Q ranges (Supporting Information Figures S2 and S3).

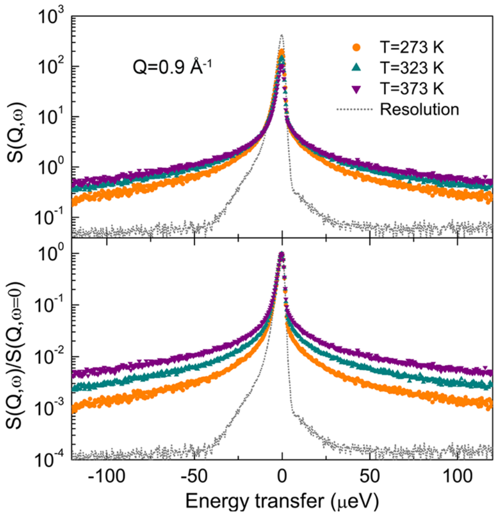

Figure 3. Representative BASIS spectra of subtracted doped *d*-P3HT at $Q = 0.9$ Å $^{-1}$ at 273 K (orange), 323 K (dark cyan), and 373 K (purple), along with the resolution function obtained at 50 K (gray dashed line). Both unnormalized (top) and normalized (bottom) data with respect to their intensity at $\hbar\omega = 0$ are shown.

In order to extract diffusive information from QENS, the experimental spectra were fit using a model function discussed in the Data Analysis section (eqs 1 and 2). Again, since two dynamic processes are observed above 254 K, two stretched exponential relaxation (or Kohlrausch−Williams−Watts, KWW) functions were included in the quasi-elastic term $S_{\mathrm{qe}}(Q,\omega)$ in eq 2, expressed as

$$S_{\mathrm{qe}}(Q,\,\omega) = P\int \exp\left[-\left(\frac{t}{\tau_1}\right)^{\beta_1}\right]\exp\left(i\frac{E}{\hbar}t\right)\mathrm{d}t + (1-P)\int \exp\left[-\left(\frac{t}{\tau_2}\right)^{\beta_2}\right]\exp\left(i\frac{E}{\hbar}t\right)\mathrm{d}t \quad (3)$$

where τ and β are the characteristic time and stretching exponent, respectively, while the subscripts 1 and 2 represent different dynamic components. The parameter P is defined as the fraction of the first Fourier-transformed stretched exponential relaxation term. E is the energy change of the neutrons, and $\hbar$ is the reduced Planck constant. Using this model, we expect that the rotations of methyl group can be captured by the faster stretched exponential term (set $\tau_1 < \tau_2$),

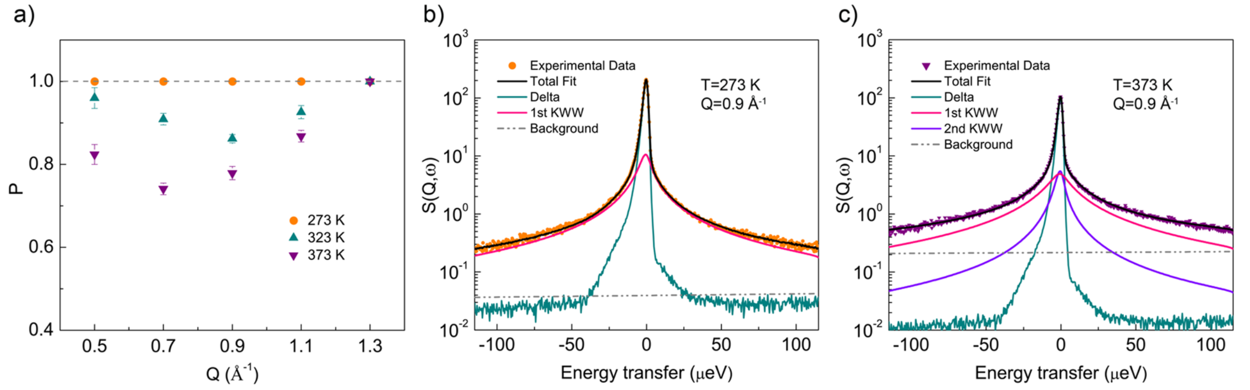

Figure 4. (a) Relative weight of the first KWW term (eq 3) as a function of Q at various temperatures. (b) Representative QENS spectrum and fit with a single KWW function of subtracted doped *d*-P3HT at a Q of 0.9 Å^{-1} and temperature of 273 K. (c) Representative QENS spectrum and fits with two KWW functions of subtracted doped *d*-P3HT at a Q of 0.9 Å^{-1} and temperature of 373 K.

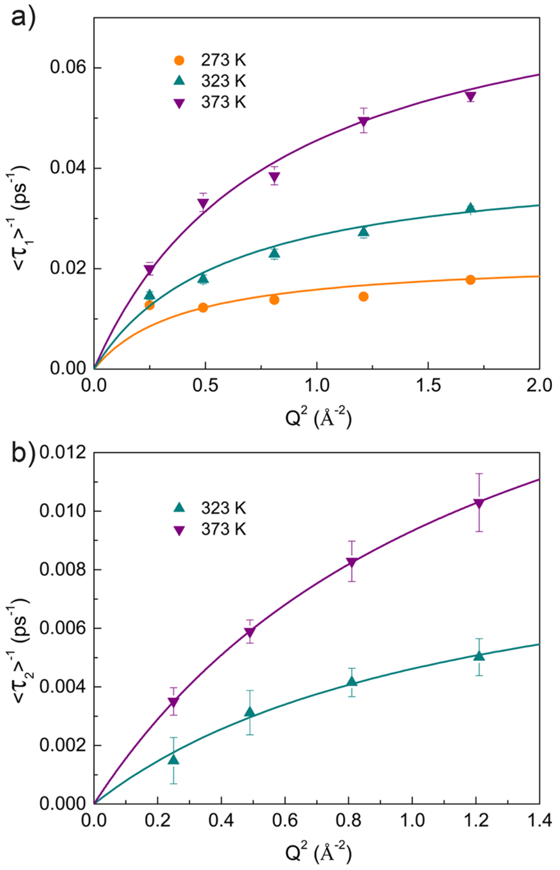

Figure 5. Inverse of mean relaxation time (symbols) of the fast process (a) and slow process (b) obtained from KWW fits as a function of Q^2 at various temperatures. The corresponding solid lines are the best representative fits to the jump diffusion model.

while the other motion of the hydrogen sites can be captured using the slower stretched exponential term.

We performed fits to all the spectra and found that a single stretched exponential term was sufficient for satisfactory fits of the 273 K data (the fit weight P values converge to unity, shown in Figure 4a), but at 323 and 373 K, fitting $S_{qe}(Q,\omega)$ required incorporating two KWW terms for all data except Q = 1.3 Å^{-1}. Examples of these one and two KWW fits are presented in Figures 4b and 4c, respectively. As can be seen, the fits capture the experimental spectra reliably over the entire energy range in both cases. We attribute the successful fit using only one KWW term at 273 K to the fact that the dynamics of methyl group rotations dominate at a temperature that is just slightly above 254 K. Reduced P values, therefore, are expected once temperature increases, which is exactly what is observed. The P values follow a clear decreasing trend upon heating. At 373 K, an average of ∼20% of the total inelastic hydrogen scattering is due to the second dynamic process. The full experimental spectra and fits at all conditions are shown in Supporting Information Figures S4−S6.

The successful fits of QENS spectra using a stretched exponential model allow us to further explore the nature of the dynamic motions. Normally, the mean relaxation time $\langle\tau_i\rangle$ of process i is extracted by

$$\langle \tau_i \rangle = \frac{\tau_i}{\beta_i}\Gamma\left(\frac{1}{\beta_i}\right) \tag{4}$$

where τ_i and β_i are fitting parameters from the stretched exponential model in eq 3, and $\Gamma(x)$ is the gamma function. The Q^2 dependence of calculated values in the form of $\langle\tau_i\rangle^{-1}$ is plotted in Figure 5. The comparison of absolute $\langle\tau_i\rangle^{-1}$ values clearly implies that two distinct diffusive motions are observed as expected. In addition, Figure 5 shows that for both fast and slow processes the $\langle\tau_i\rangle^{-1}$ values exhibit a quadratic behavior at low Q values and then a saturation trend at high Q values. This nonlinear variation of $\langle\tau_i\rangle^{-1}$ as a function of Q^2 indicates noncontinuous diffusion of hydrogen sites,[54] which is particularly true for the case of methyl group rotations. Therefore, a well-studied jump diffusion model (Singwi−Sjölander model) was employed to describe both dynamic processes, given by[55]

$$\frac{1}{\langle\tau\rangle} = \frac{DQ^2}{1 + DQ^2\tau} \tag{5}$$

where τ is the residence time between jumps of a diffusive particle and D is the diffusion coefficient. The mean-square jump length can also be determined by $\langle L^2\rangle = 6D\tau$ in this model. As can be seen from the solid lines in Figure 5, these fits yield a reasonable agreement with the data, and the resulting diffusion parameters at each temperature are summarized in Table 1.

By comparing the two dynamic processes, we notice that the observed diffusion coefficients of the faster process are approximately 1 order of magnitude greater than those of the

Table 1. Model Parameters Obtained from Fits of the Q^2-Dependent $\langle\tau_1\rangle^{-1}$ and $\langle\tau_2\rangle^{-1}$ Using a Jump Diffusion Model

	temp (K)	diffusion coeff D ($\times10^{-6}$ cm^2/s)	residence time τ (ps)	mean jump length ($\langle L^2\rangle)^{1/2}$ (Å)
fast process	273	3.13 ± 1.05	34.38 ± 8.50	2.54 ± 0.74
	323	5.90 ± 0.90	20.23 ± 1.62	2.68 ± 0.31
	373	10.17 ± 0.89	12.13 ± 0.64	2.72 ± 0.19
slow process	273			
	323	0.86 ± 0.12	100.15 ± 18.01	2.27 ± 0.26
	373	1.68 ± 0.15	46.57 ± 10.22	2.17 ± 0.34

slower process. Also, the residence time values are factor of 5 lower at the same temperature for the faster process. The mean jump lengths, on the other hand, are comparable at 2−3 Å. With respect to the individual process, the rotational diffusion coefficient of the methyl group increases from 3.13 × 10^{-6} cm^2/s at 273 K to 10.2 × 10^{-6} cm^2/s at 373 K. Although we are unable to capture the slower motion process at 273 K, the diffusion coefficient of the second dynamic process still exhibits a 2-fold increase from 323 to 373 K.

Further analysis of the temperature dependence of the diffusion coefficients and residence time was performed. Here, Arrhenius behavior was assumed to fit the data (seen in Figure 6) and an activation energy E_A associated with each process was determined, which is summarized in Table 2. As can be seen, the activation energy of the slow process (∼14 kJ/mol) is slightly higher than that of the fast process (∼10 kJ/mol).

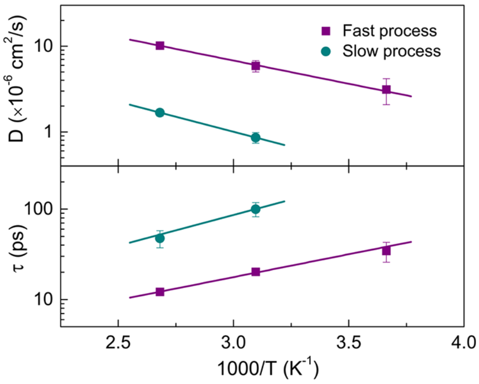

Figure 6. Diffusion coefficient (top) and residence time (bottom) as a function of 1000/T for the first dynamic (purple circles) and second dynamic (dark cyan squares). The corresponding solid lines are fits to an Arrhenius behavior.

Table 2. Activation Energy E_A (kJ/mol) Obtained from Arrhenius Fits of Diffusion Coefficient D and Residence Time τ Associated with Dynamics of Hydrogen Atoms[a]

	E_A from diffusion coeff (kJ/mol)	E_A from residence time (kJ/mol)	E_A from elastic scattering (kJ/mol)
fast process	10.4 ± 0.5	9.6 ± 0.8	7.0 ± 0.3
slow process	13.4 ± 2.8	14.9 ± 4.4	

[a] The E_A value derived from elastic scattering is also shown for comparison.

Generally, the E_A of methyl group rotation is reported to be 6−12 kJ/mol for small molecules[56−58] and polymers.[51,59−61] To more accurately determine the E_A for this specific sample, we first performed density-functional theory (DFT) calculations on an isolated dopant molecule. The F4MCTCNQ methyl hydrogens were rotated through 120° in 30° increments with the rest of the atoms in the system fixed. As can be seen in Figure 7b (orange curve), the energy barrier to methyl rotation occurs at a 60° offset from the global minimum energy configuration. The calculated barrier of ∼4 kJ/mol is roughly consistent with the experimental barrier of ∼10 kJ/mol. However, since this calculated energy barrier could also be affected by the P3HT chains, the barrier in the presence of fixed chains was investigated, and the actual barrier is likely to be between these values. We assumed here, based on the published geometry of P3HT in the presence of F4TCNQ,[62,63] that a F4MCTCNQ molecule is sandwiched between two M8 chains as seen in Figure 7a. Given the possible sensitivity to the M8 chain distance, calculations at two distinct intermolecular separations (6.30 and 6.96 Å) were performed. Figure 7b shows that the magnitude of the rotational barrier increases slightly with increasing interchain separation. In both cases, the barrier to methyl rotation was determined to be 8−10 kJ/mol, yielding a linear distance of 1.8 Å and arc length of 2.1 Å for moved hydrogen atom in this rotation. Given the typical errors of this type of calculation of at least 1 kcal/mol (∼4 kJ/mol), this result is consistent with the QENS experiments. The value of the jump length, however, is a slightly lower than that determined experimentally, which could be due to the approximations made in the calculations, which were performed in vacuum at zero temperature and with fixed positions for the thiophene backbone. The good match between QENS experiments and DFT calculations validate the assignment of the fast dynamic process to the methyl rotation of F4MCTCNQ.

With regard to the slower observed motion, we can confidently rule out based on DFT calculations that it is due to the translational diffusion of F4MCTCNQ along the polymer backbone. Figure 7c shows the calculated energy profile for the translation of a F4MCTCNQ molecule for one thiophene unit (∼4 Å) in each direction from its lowest energy position for the 6.96 Å separation and half a thiophene unit (∼2 Å) in each direction for the 6.30 Å separation. The closer interchain distance between thiophene chains yields substantially higher energy barriers to translation in both directions (∼60 kJ/mol). However, even calculation using a larger interchain separation still yields a large energy barrier of ∼30 kJ/mol. Extending the translation for the larger interchain distance to one thiophene unit demonstrates local minima at every half-thiophene unit translation, corresponding to F4MCTCNQ ring stacking directly over a thiophene ring. In any case, the calculated translational barriers are considerably higher than what were measured experimentally from QENS (∼14 kJ/mol).

Given the small activation energy and jump length of the slower motion, it seems more reasonable that this motion is associated with a localized motion that is internal to the F4MCTCNQ molecule. Closer inspection of the translation calculations in Figure 7c implies that low-energy vibrational motion around the position minima may be responsible for the slower motion. In other words, the whole F4MCTCNQ molecule might move back and forth within a potential well. However, further calculations using a simple harmonic

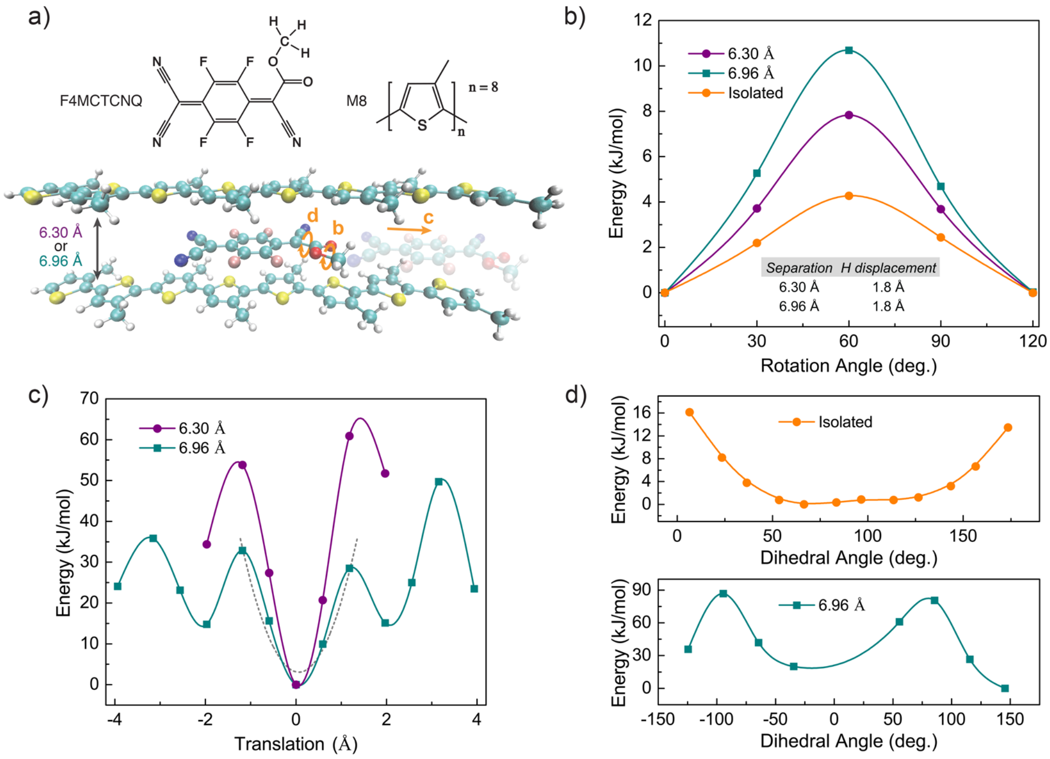

Figure 7. (a) Sandwich geometry comprising two M8 oligomers and a F4MCTCNQ molecule. The corresponding diffusive motions of each DFT calculations are also described schematically. (b) Rotation energy of the ester methyl hydrogens through 120° for two interchain separations and the isolated dopant molecule. Inset: calculated hydrogen displacements for the F4MCTCNQ methyl rotation. (c) Translation energy of the monoester molecule over one thiophene unit (6.30 Å interchain separation) and two thiophene units (6.96 Å interchain separation). The dashed gray line is the quadratic fit in order to yield a harmonic potential. (d) Rotation energy of ester group for the isolated dopant molecule (top) and a 6.96 Å interchain separation (bottom).

oscillator model, shown as the dashed gray line in Figure 7c, enable us to disprove this hypothesis. The calculated energy spacing between vibrational energy levels (~2.5 meV, Supporting Information section 6) is significantly higher than the energy spread of the QENS measurements (on the order of μeV), indicating that it is impossible to capture this dynamic motion in the energy window on BASIS. Other possible sources of the slower motion are the localized rotation of methoxycarbonyl group ($-COOCH_3$) or the rotation of methoxy group ($-OCH_3$) in F4MCTCNQ. We can safely rule out the methoxy rotation assignment because of its high rotation barrier (>50 kJ/mol) in the literature calculations even for an isolated molecule.[64,65] On the other hand, DFT calculations of the methoxycarbonyl rotation of an isolated F4MCTCNQ molecule (Figure 7d) yields a barrier of ~16 kJ/mol, which is consistent with the QENS results. Although the calculation on the sandwich geometry (6.96 Å interchain separation) produces a significantly higher barrier, a lower value wound be expected if the relaxation of the chains were allowed. In addition, given the fact that the inferred E_A values of the slower motion are in good agreement with reported values for methoxycarbonyl rotations,[65] we tentatively assign the slower motion to this rotation of the dopant.

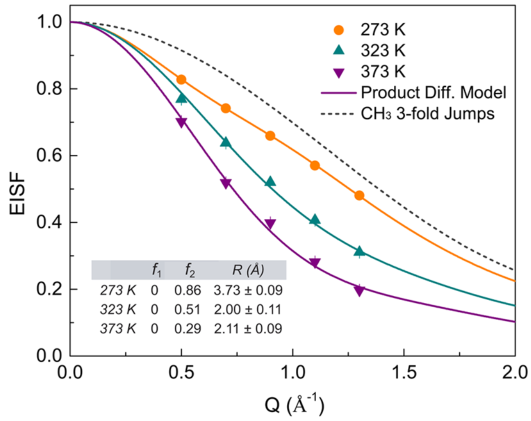

Figure 8. Elastic incoherent structure factor (EISF) obtained for subtracted doped *d*-P3HT as a function of *Q* at 273 K (orange), 323 K (dark cyan), and 373 K (purple). The solid lines are product fits to a rotational jump diffusion on a circle model (set $N = 30$ in eq 7) and a methyl group 3-fold jump model. The 3-fold jump model of the methyl group is also shown for comparison. Inset: obtained EISF fit parameters using the product diffusion model in form of eq 7.

Additional insight, particularly into the geometry of the motion, can also be obtained by investigating the elastic incoherent structure factors (EISF). The *Q*-dependent EISF values at three investigated temperatures are plotted in Figure 8. A 3-fold jump model has been widely used to describe methyl group rotations:[66,67]

$$\mathrm{EISF}_{\mathrm{methyl}}(Q) = f_1 + (1 - f_1)\left(\frac{1}{3}[1 + 2j_0(\sqrt{3}\,Qr)]\right) \quad (6)$$

where j_0 is the spherical zeroth-order Bessel function, f_1 is the fraction of immobile protons, and r is the radius, which was set to 1.03 Å based on the known geometry of methyl group.[68] However, the fit of methyl group 3-fold jumps (dashed line) shows significant deviation from the EISF values and is also

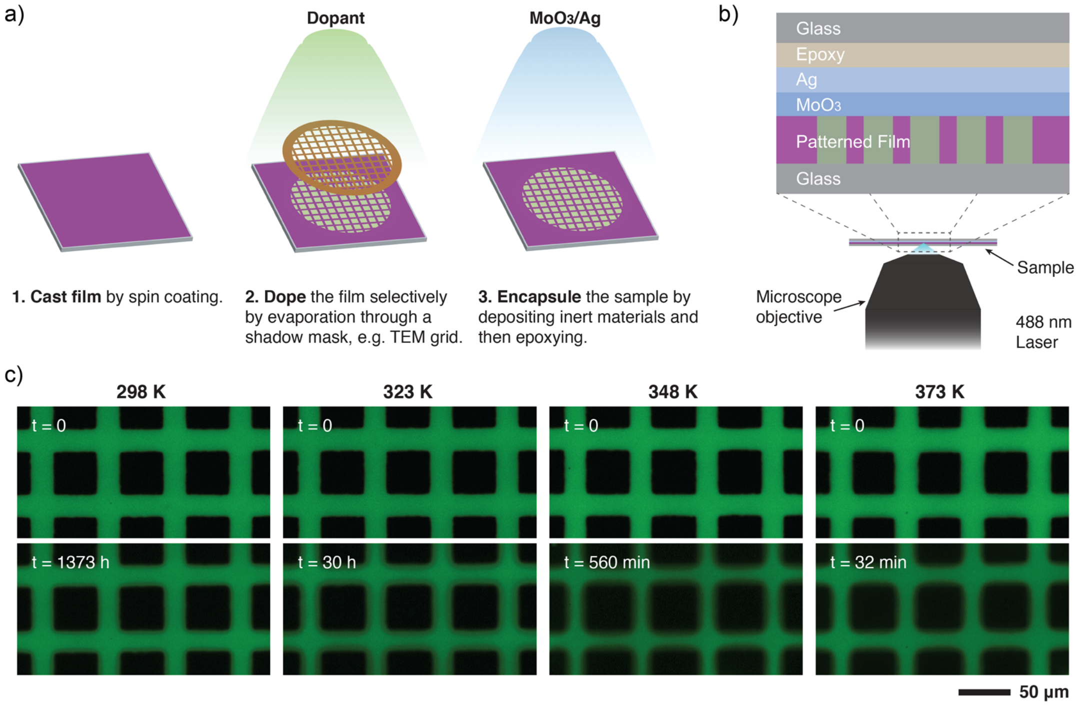

Figure 9. Schematics of (a) sample preparation and (b) resulting sample geometry and confocal experimental setup. (c) The confocal fluorescence images of patterned films before (top row) and after (bottom row) annealing at various temperatures (298, 323, 348, and 373 K) for time *t*.

greater in all cases. This clearly indicates that the methyl group rotation is not the only component that contributes to the QENS signal even at 273 K and that the slower motion must also be taken into account, which again is in good agreement with our observations from the elasitic QENS data. Therefore, we rewrite eq 6 by including a well-established rotational diffusion model, where it is assumed that the scattering center jumps between N equivalent points on a circle:[69,70]

$$\mathrm{EISF}(Q) = \left[f_1 + (1 - f_1)\left(\frac{1}{3}[1 + 2j_0(\sqrt{3}\,Qr)]\right)\right] \times \left[f_2 + (1 - f_2)\left(\frac{1}{N}\sum_{i=1}^{N} j_0\left(2QR\,\sin\frac{\pi i}{N}\right)\right)\right] \quad (7)$$

where f_2 is the fraction of immobile protons involved in the methoxycarbonyl rotation, R is the circle radius, and r is still set to 1.03 Å. The product form means that the whole methyl group moves during the methoxylcarbonyl rotation. The detailed derivation is shown in Supporting Information section 1. For $N \rightarrow \infty$, the limiting case of continuous rotational diffusion on a circle is reached. By means of this improved model, the EISF behavior is able to be captured over the whole investigated Q range as seen the solid lines in Figure 8 where N is set to 30 (a satisfactory fit is found for $N \geq 2$). In all cases, the parameter f_1 always converges to 0, revealing that all hydrogen sites are involved in the methyl rotations at any given temperature. The parameter f_2 and R, on the other hand, are found to vary slightly and converge with increasing N (Figure S7), the corresponding converged values of which are summarized in the inset of Figure 8. As can be seen, the values of f_2 follow a clear decreasing trend from 0.86 to 0.29 upon heating, which is consistent with results from Figure 4 that increased scattering from the slower motion is observed as temperature increases. Moreover, the diffusive motion of the slower motion is restricted on a circle of ~2.0−3.7 Å radius, which is also consistent with the geometry of the methoxycarbonyl rotation, where the distance from the center of methyl hydrogen sites to the rotation axis is estimated to be ~1.7 Å.

Part Two: Macroscopic Dynamics of Molecular Dopants. The previous section demonstrated that two molecular-scale motions of F4MCTCNQ in P3HT can be observed and assigned from QENS experiments. Unfortunately, the energy window of the BASIS spectrometer was insufficient to observe rarer and longer-range diffusive processes that contribute to macroscopic diffusion. Therefore, laser scanning confocal microscopy (LSCM) was used to quantify the macroscopic diffusion of F4MCTCNQ in P3HT.

In order to make this macroscopic measurement possible, a specific sample architecture was required, which was derived from our recently developed dopant-induced solubility control (DISC) patterning method.[13] Schematics of the sample preparation and resulting sample geometry are shown in Figures 9a and 9b, respectively, and a detailed sample description is provided in the Experimental Section. It is worth emphasizing that it is very important to insert a MoO_3 (or similarly performing oxide) layer between the patterned film and the Ag layer in this experiment because the high work function MoO_3 (WF = 6.8 eV) can act as an insulator to prevent dopant−metal reactions.[71] It is also well-known that the fluorescence (FL) of P3HT is quenched by the presence of dopants or any electron-accepting molecules.[72−75] By mapping out the FL intensity from LSCM and combining with a calibration curve (Figure S8), we were able to track the dopant concentration in the P3HT film spatially and temporally. We assumed here that there was no vertical concentration gradient of dopants, and thus all diffusion occurs within the two-dimensional plane of the P3HT film. This assumption is valid considering that the P3HT film is only 50 nm thick and fluorescence is measured spatially over ~1−10 μm. Figure 9c

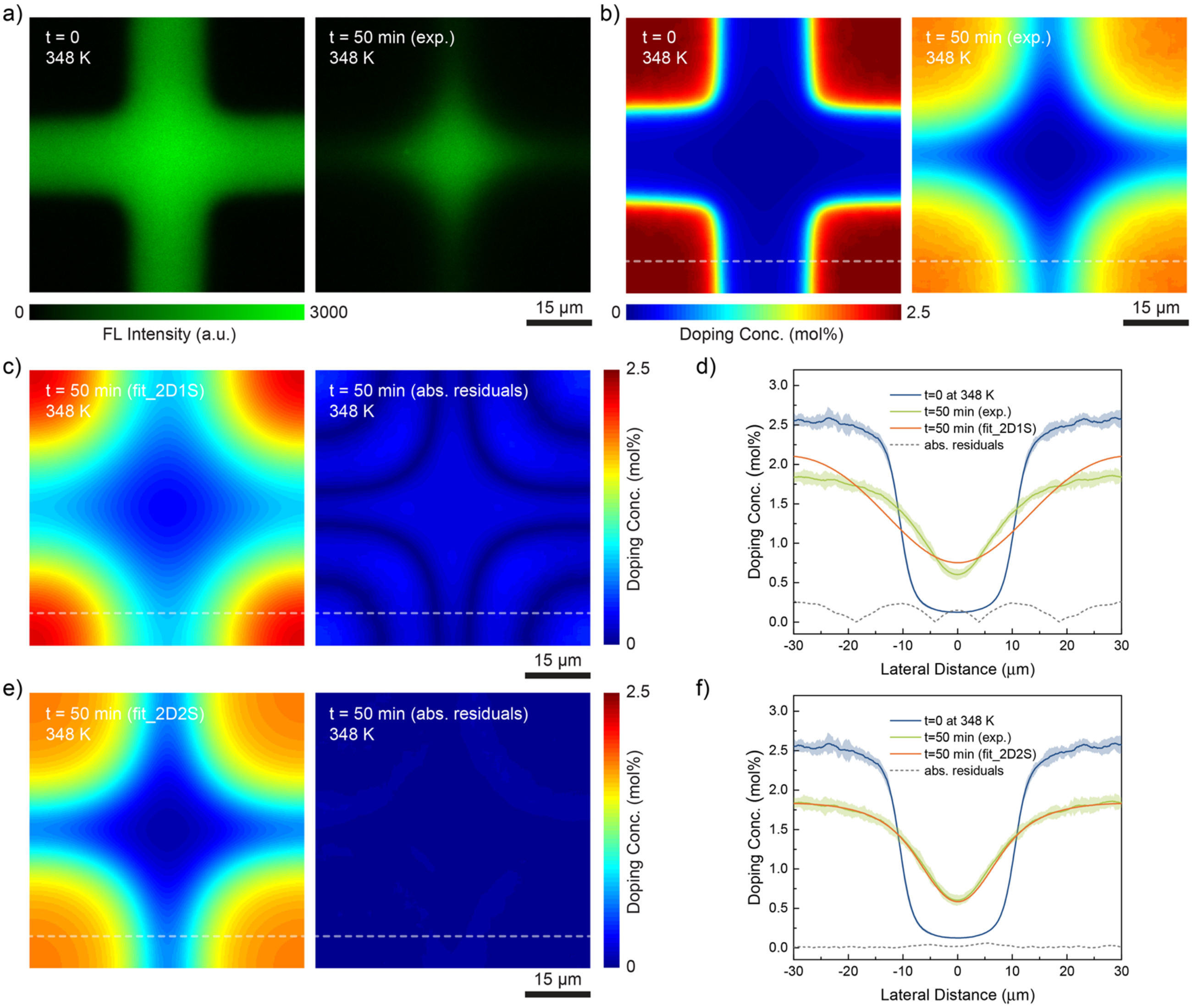

Figure 10. (a) LSCM fluorescence images of patterned F4TCNQ/P3HT films before (left) and after (right) annealing at 348 K for 50 min. (b) The 2D doping concentration maps converted from LSCM fluorescence images using a calibration curve at t = 0 (left) and t = 50 min (right). (c) The 2D doping concentration maps for a two-dimensional one-species (2D1S) model fit (left) and its absolute residuals (right). (d) Cross-sectional doping concentration profiles through images in (b) and (c) (indicated by white dashed lines) using a 2D1S diffusion model. (e) The 2D doping concentration maps for a two-dimensional two-species (2D2S) model fit (left) and its absolute residuals (right). (f) Cross-sectional doping concentration profiles through images in (b) and (e) (indicated by white dashed lines) using a 2D2S diffusion model.

show examples of confocal FL images before (top) and after (bottom) annealing for a time t at four different temperatures. The narrowing gaps in the FL intensity clearly indicate that the F4MCTCNQ diffuses from the doped (dark) regions to the undoped (bright) regions in the sample over time, as expected. Preliminary analysis based upon the annealing time at the different temperatures suggests that the macroscopic diffusion rate of the dopant is at least 1 order of magnitude higher for every 25 K temperature increase from 298 to 373 K.

We quantified the macroscopic diffusion rate and mechanism by fitting the dopant concentration as a function of lateral position and diffusion time. The F4TCNQ/P3HT system was used to validate our models. Initially, we attempted to fit the data by using a one-dimensional (1D) Fickian diffusion model that has been used previously to determine the diffusion coefficient of PCBM in a P3HT film,[20] the details of which are shown in Figure S9. This 1D model dose not successfully capture the F4TCNQ diffusion behavior. Therefore, we extended this 1D model to a two-dimensional, one-species (2D1S) diffusion model, which appeared to be more realistic. Images of 60 × 60 μm were used for all the fits in order to save computational time. The experimental confocal FL images before and after annealing at 348 K for 50 min and converted to 2D doping concentration maps are presented in Figures 10a and 10b, respectively, both of which clearly show F4TCNQ diffusion. For this 2D1S model, only one diffusive species was taken into account. The model fit and corresponding residuals are shown in Figure 10c. A direct comparison of cross-sectional profiles from these experimental and fitting images (indicated by the white dashed lines in Figures 10b and 10c, respectively) is also shown in Figure 10d. Again, a single diffusing species model yields an unsatisfactory fit for dopants concentration versus temperature and time, which can be seen from the discrepancy between measured (green line) and fit (red line) doping levels.

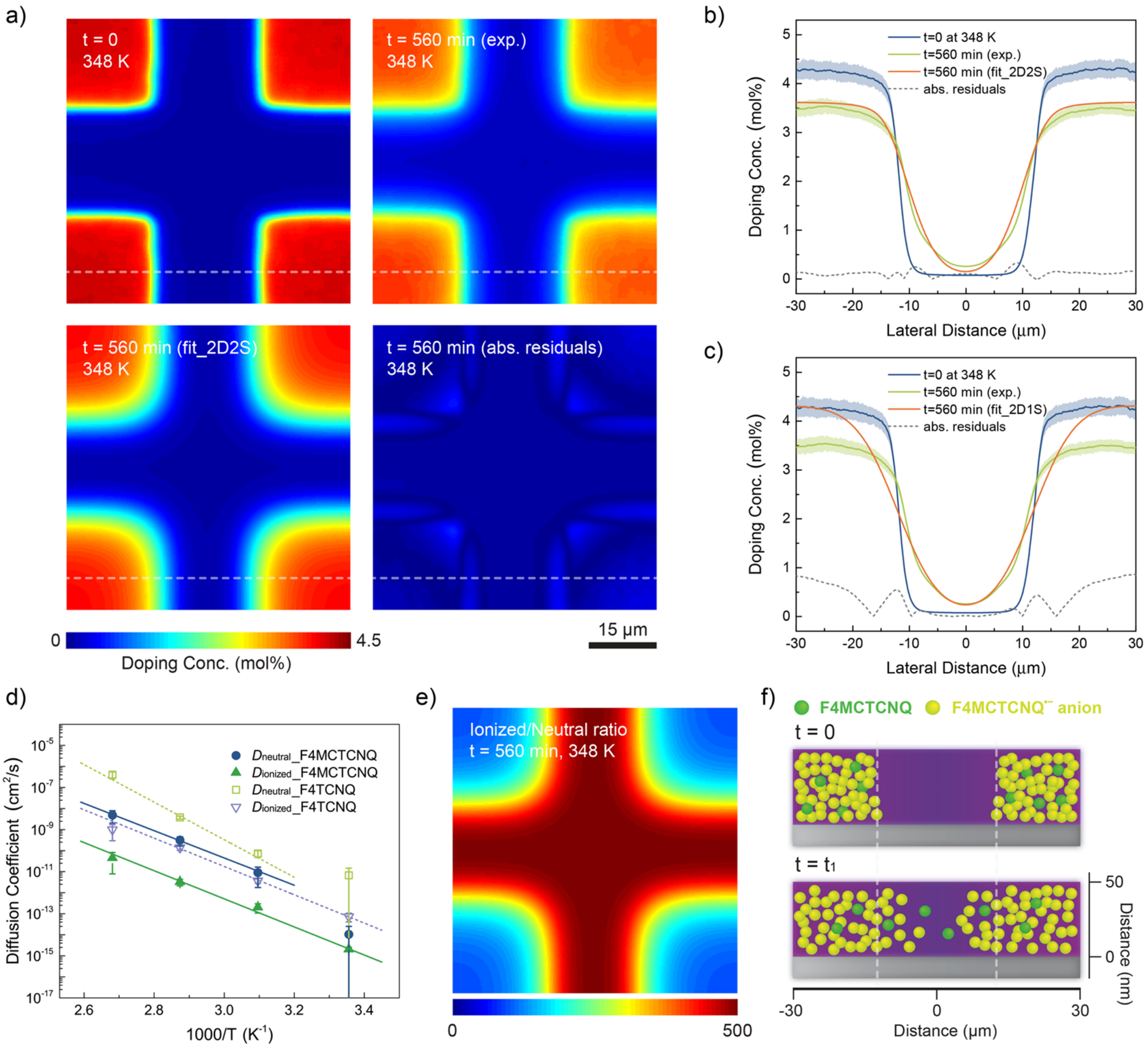

Figure 11. (a) A representative F4MCTCNQ diffusion fit at 348 K using a two-dimensional two-species (2D2S) model. 2D doping concentration maps were obtained experimentally from LSCM at $t = 0$ (top left) and $t = 560$ min (top right), 2D2S fit (bottom left), and absolute residuals (bottom right). (b) Cross-sectional doping concentration profiles through images in (a) (indicated by white dashed lines) using a 2D2S diffusion model. (c) Cross-sectional doping concentration profiles using a two-dimensional one-species (2D1S) diffusion model. (d) Determined two diffusion coefficients from 2D2S fits as a function of annealing temperatures for F4MCTCNQ (solid symbols) and F4TCNQ (open symbols) as well as corresponding Arrhenius fits. (e) 2D mole ratio profiles of slower (ionized) species to faster (neutral) species at $t = 560$ min at 348 K for F4MCTCNQ diffusion. (f) Schematic of F4MCTCNQ dopant diffusion derived from 2D2S diffusion model analysis.

We recently showed that an equilibrium between neutral F4TCNQ and ionized F4TCNQ exists in sequentially processed doped P3HT films, which can be described by F4TCNQ + P3HT $\rightleftharpoons$ F4TCNQ$^-$ + P3HT$^+$.[14] In the cited study, F4TCNQ was added into the P3HT film using an orthogonal solvent. We showed that the orthogonal solvent could not dissolve or deposit F4TCNQ into the crystalline domains of P3HT, but instead only doped the amorphous domains of the polymer. In addition, we quantified the site density versus doping level for doping of the amorphous P3HT using a Langmuir isotherm model. We posit that the same model is very likely to explain the equilibrium for the F4TCNQ dopant in evaporation patterned P3HT films. The Langmuir isotherm model can be expressed as

$$\theta = \frac{C_{\mathrm{ionized}}}{C_{\mathrm{sat}}} = \frac{K_{\mathrm{eq}} C_{\mathrm{neutral}}}{1 + K_{\mathrm{eq}} C_{\mathrm{neutral}}} \quad (8)$$

where θ is the fraction of occupied doping sites in the amorphous domains of the film, C_{ionized} is the film doping concentration, C_{sat} is the saturated film doping concentration, C_{neutral} is the concentration of neutral dopant molecules, and K_{eq} is the equilibrium constant.

Given that both neutral and ionized dopants coexist in this sample, we developed a two-dimensional two-species (2D2S) diffusion model assuming (1) that the neutral and ionized species obey the aforementioned Langmuir isotherm equilibrium and (2) that the rate of equilibration between the two species is much faster than the rate of diffusion. Since increasing the temperature would shift the equilibrium toward a higher population of neutral dopants, the temperature-dependent $K_{\mathrm{eq}} = \exp(-\Delta G^\circ/(k_B T))$, where ΔG° is taken to be the HOMO−LUMO difference between P3HT and the dopant (i.e., roughly the change in energy of the charge transfer process; 0.23 eV for F4TCNQ and 0.14 eV for F4MCTCNQ[36]), k_B is the constant, and T is the temperature. The 2D mapped doping concentration profiles were then fit with a 2D solution to Fick's second law, yielding a diffusion coefficient for each diffusive species (denoted as D_{neutral} and D_{ionized} in order to differentiate them from the diffusion coefficients obtained from QENS). The performed 2D2S fit for the F4TCNQ diffusion at 348 K is shown in Figure 10e. By comparing the experimental and fit doping concentration profiles and inspecting the low residual between the data and fit in Figures 10b and 10e, it is clear that this 2D2S model is able to reproduce the lateral diffusion rates and mechanism in a consistent manner. Cross-sectional profiles through these images (indicated by the white dashed lines) are shown in Figure 10f and directly compared with the 2D2S fit. A full comparison between 2D1S and 2D2S model fits for F4TCNQ diffusion at other investigated temperatures can be found in Figures S10 and S11.

This 2D2S diffusion model was applied to describe the diffusion of F4MCTCNQ in the P3HT films. A representative example of the 2D2S fit for F4MCTCNQ at 348 K is shown in Figure 11a, and the cross-sectional doping concentration profiles through these images are provided in Figure 11b. The fits at other investigated temperatures can be found in Figure S12. Similar to the case of F4TCNQ, satisfactory fits can be produced. For consistency, the 2D1S model fits on F4MCTCNQ were also performed, and the resulting cross-sectional profiles at the same position are shown in Figure 11c (corresponding 2D images are presented in Figure S13). The discrepancy between measured and fit doping levels, especially in the doped region, using the 2D1S model again shows that a two species diffusion model is necessary to fit the diffusion data with sufficient accuracy. Additionally, since the highest doping ratio of ~4.3 mol % in the feature centers is much lower than the reported saturated doping level (>17 mol %),[36,62] it is reasonable to assume that ionized dopants are the majority of the diffusive species in the system. Also, since the highest doping ratio is below the C_{sat} determined for the amorphous domains of P3HT in the previous study,[14] it is likely that most or all of the dopants are located in and transported through the amorphous domains of P3HT.

The resulting two diffusion coefficients of the faster and slower species obtained from the 2D2S diffusion model are plotted as a function of the inverse of the annealing temperatures (1000/T) in Figure 11d. As can be seen, two distinct diffusion coefficients are observed. The diffusion coefficient of the faster species D_{neutral} is approximately 2−3 orders of magnitude greater than that of the slower species D_{ionized} at the same temperature for both the F4MCTCNQ and F4TCNQ dopants in P3HT. Since the Langmuir isotherm model tracks the number of available doping sites in the P3HT, it is reasonable that the ratio of ionized to neutral dopants increases with reduced doping density. The mole ratio of the ionized (slower) to neutral (faster) dopant species is therefore tracked in this diffusion model. A representative 2D map of the ionized/neutral doping ratio for F4MCTCNQ/P3HT at 348 K is shown in Figure 11e. It is clear that the concentration of neutral species is orders of magnitude lower than the ionized species (also seen in Figure S14) and that this ratio is position-dependent, reflecting the local equilibrium between unfilled P3HT sites and dopants. Additionally, the ratio of ionized to neutral molecules increases as a function of diffusion distance, from ~100 in the initially doped region to ~500 in the initially undoped region (Figure S14). This increased ratio implies that the neutral dopant can diffuse for longer times in the highly doped part of the sample, where there are fewer free undoped sites on the P3HT. As the dopant leaves the highly doped region, the neutral dopant is presented with a large number of free doping sites and so readily binds. The two-species diffusion processes is illustrated schematically in Figure 11f.

Since the temperature-dependent diffusion coefficients follow, within error, Arrhenius behavior (the straight lines in Figure 11d), we are able to determine the activation energy E_A associated with the diffusion process for each species. In our calculations, the D_{neutral} values at 298 K are excluded due to their uncertainties, seen from the large error bars in Figure 11d. The determined E_A values for translational diffusion are listed in Table 3. Interestingly, the E_A values for both neutral and ionized F4MCTCNQ (~55 kJ/mol) are consistent with the translational barriers from DFT calculations in Figure 7c (especially for the smaller interchain separation). We note that the jump distance for an ionized dopant depends strongly on the energy landscape. As can be seen from Figure 7c, an open site (no other dopant in the path) and sufficient energy to surmount a 50−60 kJ/mol barrier for hopping to the next site are required for the ionized species to jump into the nearby potential well that is one bond. In addition, Kramer's theory was applied to estimate the diffusion coefficient of the dopant based on the DFT potential energy curves (Supporting Information section 11). The calculation yields a diffusion coefficient for ionized F4MCTCNQ of 1.4×10^{-14} cm^2/s at 298 K, which again falls into the range measured in the confocal experiments. However, the geometry of the DFT calculations depicted a highly simplified ordered P3HT domain, which is likely to different from the amorphous P3HT domain in which the dopant is expected to reside at the doping density used in the experiment. Given this discrepancy between the simulated geometry and likely sample geometry, we speculate that the measured E_{A_ionized} likely represents an average value and that the actual hopping barriers in amorphous domains will be more heterogeneous than those estimated in the DFT calculations.

Table 3. Activation Energy E_A (kJ/mol) for Translational Diffusion Obtained from Arrhenius Fits of Diffusion Coefficients (D_{neutral} and D_{ionized}) of Neutral and Ionized Dopant Molecules, Respectively[a]

	E_{A_neutral} (kJ/mol)	E_{A_ionized} (kJ/mol)
F4MCTCNQ	53.8 ± 1.9	55.5 ± 2.4
F4TCNQ	74.2 ± 7.3	55.9 ± 2.6

[a] E_A values of F4TCNQ diffusions are also shown for comparison.

In addition, we can infer from the diffusion model that the jump distance for the neutral dopant is considerably larger than for the ionized dopant, even though their activation energies are similar. We know that the neutral dopant is not Coulombically bonded to the P3HT. We also know from the comparison of the 2D1S and 2D2S models that the neutral species is needed to explain the bulk diffusion profile as a function of time and temperature. It can be seen that the jump attempt frequency for the neutral and ionized molecules are similar, since since this is related to the size of the molecule and the curvature of the potential energy surface, which are likely similar of the two species. However, the jump distance is not determined from the Arrhenius fit but rather by the availability of binding sites. For an ionized dopant, the next binding site is one thiophene unit away, and thus the jump distance is smaller. For the neutral dopant, the next binding site is on average a much larger distance so although the neutral species is a minority species and has a similar jump attempt frequency to ionized F4MCTCNQ, the macroscopic diffusion is largely driven by the diffusive motion of neutral dopant molecules.

Finally, comparing the diffusion coefficients of F4TCNQ to F4MCTCNQ, we note that F4TCNQ and F4TCNQ$^-$ respectively diffuse approximately 10−100 times faster than F4MCTCNQ and F4MCTCNQ$^-$ at investigated temperatures (Figure 11d). However, the $E_{A\_neutral}$ of F4TCNQ is shown to be higher than that of F4MCTCNQ. The reduced global diffusion of F4MCTCNQ, therefore, indicates that the methyl ester side chain on the F4MCTCNQ somehow reduces its jump distance. To pin down the reason for the reduced diffusion rate of the substituted dopant, we will present detailed comparisons of temperature-dependent as well as time-dependent diffusion coefficients between F4TCNQ and its soluble analogues in a separate and upcoming paper. In addition, examining reported diffusion studies on PCBM in the P3HT matrix, we can also conclude that the diffusions of molecular dopants F4TCNQ and F4MCTCNQ are faster than that of PCBM in the P3HT ($D = \sim 10^{-14}$ cm^2/s[76−78] and $D = \sim 10^{-11}$ cm^2/s[79] at around 413 K).

The results and model presented here represent the first detailed mechanistic study of a specific dopant diffusing in a specific semicrystalline semiconducting polymer. The results and model could be applicable to a wider and more general model for dopant diffusion in a wide variety of organic semiconductors. For this model to be generally applicable, a large number of different dopants would need to be investigated in a large number of different semiconductors. Also, a general means to determine the temperature-dependent binding energies for dopants and the energy landscape for OSCs is needed.

■ CONCLUSION

In conclusion, we have unveiled the diffusion dynamics of the p-type dopant, F4MCTCNQ, in the semiconducting polymer P3HT for both microscopic and macroscopic time/distance scales using two different techniques. From QENS experiments, two local motions (<4 Å) are observed: methyl group rotations with $D \approx 10^{-6}$−10^{-5} cm^2/s and methoxycarbonyl group rotations with smaller $D \approx 10^{-7}$−10^{-6} cm^2/s, both of which exhibit small E_A values (<15 kJ/mol) that are confirmed by DFT calculations. The macroscopic dynamics, on the other hand, are captured by an LSCM imaging technique. A two-dimensional two-species model is developed to interpret this long-range diffusion behavior, which includes a Langmuir isotherm equilibrium between neutral and ionized dopant molecules. As the dominant species, the ionized F4MCTCNQ molecules exhibit slower diffusion than the neutral molecules due to a much shorter jump distance. Both the activation energy for diffusion and the jump distance of the ionized species are in good agreement with the estimates from DFT calculations associated with the translational motions of F4MCTCNQ along the P3HT backbone (E_A of ∼50 kJ/mol and jump distance of ∼2 Å). In contrast, the neutral species has a significantly greater jump distance, which makes the neutral species the dominant diffusing species at the macro scale. Lastly, by comparing the diffusion coefficients between F4MCTCNQ and F4TCNQ, we can also conclude that methyl ester substitution in F4MCTCNQ not only increases solubility/miscibility and thus doping effectiveness but also helps to anchor dopants into position postdeposition due to reduced diffusion. In theory, the two-dimensional one-/two-species diffusion developed in this paper could be generalized to determine the diffusion coefficient of any fluorescence quenching species that can be evaporated into a polymer. Studies of the dopant dynamics at both microscopic and macroscopic levels are important for understanding the degradation of organic devices as well as improving DISC patterning methodology.

■ ASSOCIATED CONTENT

Ⓢ Supporting Information

The Supporting Information is available free of charge on the ACS Publications website at DOI: 10.1021/acs.macromol.7b00672.

Figures S1−S14 (PDF)

■ AUTHOR INFORMATION

Corresponding Author

*E-mail: amoule@ucdavis.edu (A.J.M.).

ORCID

Jun Li: 0000-0001-7850-3722
David M. Huang: 0000-0003-2048-4500
Ian E. Jacobs: 0000-0002-1535-4608
Thomas Harrelson: 0000-0002-8689-4273
Kunlun Hong: 0000-0002-2852-5111

Notes

The authors declare no competing financial interest.

■ ACKNOWLEDGMENTS

This project was carried out with funding from the U.S. Department of Energy, Office of Basic Energy Sciences, Division of Materials Sciences and Engineering, under Award DE-SC0010419. The DFT work was undertaken with the assistance of resources and services from the National Computational Infrastructure (NCI), which is supported by the Australian Government. Computational resources provided by the University of Adelaide's Phoenix High Performance Computing service are also gratefully acknowledged. Deuterated P3HT was synthesized at the Center for Nanophase Materials Sciences, a DOE Office of Science User Facility. A portion of this research was performed at Spallation Neutron Source, a DOE Office of Sciences facility. We thank Prof. Greg Miller (UC Davis) for advice on the development of the diffusion model.

■ REFERENCES

(1) Taima, T.; Sakai, J.; Yamanari, T.; Saito, K. Doping Effects for Organic Photovoltaic Cells Based on Small-molecular-weight Semiconductors. *Sol. Energy Mater. Sol. Cells* **2009**, *93*, 742−745.

(2) Hains, A. W.; Liang, Z.; Woodhouse, M. A.; Gregg, B. A. Molecular Semiconductors in Organic Photovoltaic Cells. *Chem. Rev.* **2010**, *110*, 6689−6735.

(3) Zhou, X.; Blochwitz, J.; Pfeiffer, M.; Nollau, A.; Fritz, T.; Leo, K. Enhanced Hole Injection into Amorphous Hole-Transport Layers of Organic Light-Emitting Diodes Using Controlled p-Type Doping. *Adv. Funct. Mater.* **2001**, *11*, 310−314.

(4) Reineke, S.; Thomschke, M.; Lüssem, B.; Leo, K. White Organic Light-emitting Diodes: Status and Perspective. *Rev. Mod. Phys.* **2013**, *85*, 1245−1293.

(5) Braga, D.; Horowitz, G. High-Performance Organic Field-Effect Transistors. *Adv. Mater.* **2009**, *21*, 1473−1486.

(6) Lu, G.; Blakesley, J.; Himmelberger, S.; Pingel, P.; Frisch, J.; Lieberwirth, I.; Salzmann, I.; Oehzelt, M.; Di Pietro, R.; Salleo, A.;

Koch, N.; Neher, D. Moderate Doping Leads to High Performance of Semiconductor/insulator Polymer Blend Transistors. *Nat. Commun.* **2013**, *4*, 1588.

(7) Heeger, A. J. Semiconducting and Metallic Polymers: The Fourth Generation of Polymeric Materials (Nobel Lecture). *Angew. Chem., Int. Ed.* **2001**, *40*, 2591−2611.

(8) Lüssem, B.; Riede, M.; Leo, K. Doping of Organic Semiconductors. *Phys. Status Solidi A* **2013**, *210*, 9−43.

(9) Zhao, X.; Zhan, X. Electron Transporting Semiconducting Polymers in Organic Electronics. *Chem. Soc. Rev.* **2011**, *40*, 3728−3743.

(10) Walzer, K.; Maennig, B.; Pfeiffer, M.; Leo, K. Highly Efficient Organic Devices Based on Electrically Doped Transport Layers. *Chem. Rev.* **2007**, *107*, 1233−1271.

(11) Olthof, S.; Tress, W.; Meerheim, R.; Lüssem, B.; Leo, K. Photoelectron Spectroscopy Study of Systematically Varied Doping Concentrations in An Organic Semiconductor Layer Using A Molecular P-Dopant. *J. Appl. Phys.* **2009**, *106*, 103711.

(12) Lee, J. H.; Lee, J.; Kim, Y. H.; Yun, C.; Lüssem, B.; Leo, K. Effect of Trap States on the Electrical Doping of Organic Semiconductors. *Org. Electron.* **2014**, *15*, 16−21.

(13) Jacobs, I. E.; Li, J.; Burg, S. L.; Bilsky, D. J.; Rotondo, B. T.; Augustine, M. P.; Stroeve, P.; Moulé, A. J. Reversible Optical Control of Conjugated Polymer Solubility with Sub-micrometer Resolution. *ACS Nano* **2015**, *9*, 1905−1912.

(14) Jacobs, I. E.; Aasen, E. W.; Oliveira, J. L.; Fonseca, T. N.; Roehling, J. D.; Li, J.; Zhang, G.; Augustine, M. P.; Mascal, M.; Moule, A. J. Comparison of Solution-mixed and Sequentially Processed P3HT:F4TCNQ Films: Effect of Doping-induced Aggregation on Film Morphology. *J. Mater. Chem. C* **2016**, *4*, 3454−3466.

(15) Jacobs, I. E.; Wang, F.; Hafezi, N.; Medina-Plaza, C.; Harrelson, T. F.; Li, J.; Augustine, M. P.; Mascal, M.; Moulé, A. J. Quantitative Dedoping of Conductive Polymers. *Chem. Mater.* **2017**, *29*, 832−841.

(16) Jacobs, I. E.; Aasen, E. W.; Nowak, D.; Li, J.; Morrison, W.; Roehling, J. D.; Augustine, M. P.; Moulé, A. J. Direct-Write Optical Patterning of P3HT Films Beyond the Diffraction Limit. *Adv. Mater.* **2017**, *29*, 1603221.

(17) Tyagi, P.; Dalai, M. K.; Suman, C. K.; Tuli, S.; Srivastava, R. Study of 2,3,5,6-tetrafluoro-7,7[prime or minute],8,8[prime or minute]- tetracyano quinodimethane Diffusion in Organic Light Emitting Diodes Using Secondary Ion Mass Spectroscopy. *RSC Adv.* **2013**, *3*, 24553−24559.

(18) Dai, A.; Wan, A.; Magee, C.; Zhang, Y.; Barlow, S.; Marder, S. R.; Kahn, A. Investigation of P-dopant Diffusion in Polymer Films and Bulk Heterojunctions: Stable Spatially-confined Doping for All-solution Processed Solar Cells. *Org. Electron.* **2015**, *23*, 151−157.

(19) Treat, N. D.; Brady, M. A.; Smith, G.; Toney, M. F.; Kramer, E. J.; Hawker, C. J.; Chabinyc, M. L. Interdiffusion of PCBM and P3HT Reveals Miscibility in a Photovoltaically Active Blend. *Adv. Energy Mater.* **2011**, *1*, 82−89.

(20) Treat, N. D.; Mates, T. E.; Hawker, C. J.; Kramer, E. J.; Chabinyc, M. L. Temperature Dependence of the Diffusion Coefficient of PCBM in Poly(3-hexylthiophene). *Macromolecules* **2013**, *46*, 1002−1007.

(21) Qi, Y.; Sajoto, T.; Kröger, M.; Kandabarow, A. M.; Park, W.; Barlow, S.; Kim, E.-G.; Wielunski, L.; Feldman, L. C.; Bartynski, R. A.; Brédas, J.-L.; Marder, S. R.; Kahn, A. A Molybdenum Dithiolene Complex as p-Dopant for Hole-Transport Materials: A Multitechnique Experimental and Theoretical Investigation. *Chem. Mater.* **2010**, *22*, 524−531.

(22) Li, J.; Rochester, C. W.; Jacobs, I. E.; Friedrich, S.; Stroeve, P.; Riede, M.; Moulé, A. J. Measurement of Small Molecular Dopant F4TCNQ and C60F36 Diffusion in Organic Bilayer Architectures. *ACS Appl. Mater. Interfaces* **2015**, *7*, 28420−28428.

(23) Li, J.; Rochester, C. W.; Jacobs, I. E.; Aasen, E. W.; Friedrich, S.; Stroeve, P.; Moulé, A. J. The Effect of Thermal Annealing on Dopant Site Choice in Conjugated Polymers. *Org. Electron.* **2016**, *33*, 23−31.

(24) Fischer, F.; Hahn, T.; Bässler, H.; Bauer, I.; Strohriegl, P.; Köhler, A. Measuring Reduced C60 Diffusion in Crosslinked Polymer Films by Optical Spectroscopy. *Adv. Funct. Mater.* **2014**, *24*, 6172−6177.

(25) Tyagi, P.; Tuli, S.; Srivastava, R. Study of Fluorescence Quenching due to 2, 3, 5, 6-Tetrafluoro-7, 7′, 8, 8′-Tetracyano Quinodimethane and Its Solid State Diffusion Analysis using Photoluminescence Spectroscopy. *J. Chem. Phys.* **2015**, *142*, 054707.

(26) Zhang, L.; Zu, F.-S.; Deng, Y.-L.; Igbari, F.; Wang, Z.-K.; Liao, L.-S. Origin of Enhanced Hole Injection in Organic Light-Emitting Diodes with an Electron-Acceptor Doping Layer: p-Type Doping or Interfacial Diffusion? *ACS Appl. Mater. Interfaces* **2015**, *7*, 11965−11971.

(27) Jung, M.-C.; Qi, Y. Dopant Interdiffusion Effects in n-i-p Structured Spiro-OMeTAD Hole Transport Layer of Organometal Halide Perovskite Solar Cells. *Org. Electron.* **2016**, *31*, 71−76.

(28) Gao, W.; Kahn, A. Controlled P Doping of the Hole-transport Molecular Material N,N-diphenyl-N,N-bis(1-naphthyl)-1,1-biphenyl-4,4-diamine with Tetrafluorotetracyanoquinodimethane. *J. Appl. Phys.* **2003**, *94*, 359−366.

(29) Kolesov, V. A.; Fuentes-Hernandez, C.; Chou, W.-F.; Aizawa, N.; Larrain, F. A.; Wang, M.; Perrotta, A.; Choi, S.; Graham, S.; Bazan, G. C.; Nguyen, T.-Q.; Marder, S. R.; Kippelen, B. Solution-based Electrical Doping of Semiconducting Polymer Films over a Limited Depth. *Nat. Mater.* **2016**, advance online publication.

(30) Gao, Z. Q.; Mi, B. X.; Xu, G. Z.; Wan, Y. Q.; Gong, M. L.; Cheah, K. W.; Chen, C. H. An Organic P-type Dopant with High Thermal Stability for an Organic Semiconductor. *Chem. Commun.* **2008**, 117−119.

(31) Gao, W.; Kahn, A. Controlled P-doping of Zinc Phthalocyanine by Coevaporation with Tetrafluorotetracyanoquinodimethane: A Direct and Inverse Photoemission Study. *Appl. Phys. Lett.* **2001**, *79*, 4040−4042.

(32) Dai, A.; Zhou, Y.; Shu, A. L.; Mohapatra, S. K.; Wang, H.; Fuentes-Hernandez, C.; Zhang, Y.; Barlow, S.; Loo, Y.-L.; Marder, S. R.; Kippelen, B.; Kahn, A. Enhanced Charge-carrier Injection and Collection via Lamination of Doped Polymer Layers p-Doped with a Solution-Processible Molybdenum Complex. *Adv. Funct. Mater.* **2014**, *24*, 2197−2204.

(33) Drechsel, J.; Männig, B.; Kozlowski, F.; Pfeiffer, M.; Leo, K.; Hoppe, H. Efficient Organic Solar Cells Based on a Double p-i-n Architecture Using Doped Wide-gap Transport Layers. *Appl. Phys. Lett.* **2005**, *86*, 244102.

(34) Meerheim, R.; Olthof, S.; Hermenau, M.; Scholz, S.; Petrich, A.; Tessler, N.; Solomeshch, O.; Lüssem, B.; Riede, M.; Leo, K. Investigation of C60F36 as Low-volatility P-dopant in Organic Optoelectronic Devices. *J. Appl. Phys.* **2011**, *109*, 103102.

(35) Lin, X.; Purdum, G. E.; Zhang, Y.; Barlow, S.; Marder, S. R.; Loo, Y.-L.; Kahn, A. Impact of a Low Concentration of Dopants on the Distribution of Gap States in a Molecular Semiconductor. *Chem. Mater.* **2016**, *28*, 2677−2684.

(36) Li, J.; Zhang, G.; Holm, D. M.; Jacobs, I. E.; Yin, B.; Stroeve, P.; Mascal, M.; Moulé, A. J. Introducing Solubility Control for Improved Organic P-type Dopants. *Chem. Mater.* **2015**, *27*, 5765−5774.

(37) Sakai, V. G.; Arbe, A. Quasielastic Neutron Scattering in Soft Matter. *Curr. Opin. Colloid Interface Sci.* **2009**, *14*, 381−390.

(38) Shao, M.; Keum, J.; Chen, J.; He, Y.; Chen, W.; Browning, J. F.; Jakowski, J.; Sumpter, B. G.; Ivanov, I. N.; Ma, Y.-Z.; Rouleau, C. M.; Smith, S. C.; Geohegan, D. B.; Hong, K.; Xiao, K. The Isotopic Effects of Deuteration on Optoelectronic Properties of Conducting Polymers. *Nat. Commun.* **2014**, *5*, 3180.

(39) Mamontov, E.; Herwig, K. W. A Time-of-flight Backscattering Spectrometer at the Spallation Neutron Source, BASIS. *Rev. Sci. Instrum.* **2011**, *82*, 085109.

(40) Azuah, R. T.; Kneller, L. R.; Qiu, Y.; Tregenna-Piggott, P. L.; Brown, C. M.; Copley, J. R.; Dimeo, R. M. DAVE: A Comprehensive Software Suite for the Reduction Visualization, and Analysis of Low Energy Neutron Spectroscopic Data. *J. Res. Natl. Inst. Stand. Technol.* **2009**, *114*, 341.

(41) Hempelmann, R. *Quasielastic Neutron Scattering and Solid State Diffusion*; Clarendon Press: 2000.

(42) Langmuir, I. The Adsorption of Gases on Plane Surfaces of Glass, Mica and Platinum. *J. Am. Chem. Soc.* **1918**, *40*, 1361−1403.

(43) Becke, A. D. Density-functional Thermochemistry. III. The Role of Exact Exchange. *J. Chem. Phys.* **1993**, *98*, 5648−5652.

(44) Grimme, S. Semiempirical GGA-type Density Functional Constructed with a Long-range Dispersion Correction. *J. Comput. Chem.* **2006**, *27*, 1787−1799.

(45) Ackling, S. Interplay of Structural, Dynamical, and Electronic Properties in Doped Semiconducting Polymer Systems. M.Sc. Thesis, The University of Adelaidem, 2017.

(46) Lemaur, V.; Steel, M.; Beljonne, D.; Brédas, J.-L.; Cornil, J. Photoinduced Charge Generation and Recombination Dynamics in Model Donor/Acceptor Pairs for Organic Solar Cell Applications: A Full Quantum-Chemical Treatment. *J. Am. Chem. Soc.* **2005**, *127*, 6077−6086.

(47) Mityashin, A.; Olivier, Y.; Van Regemorter, T.; Rolin, C.; Verlaak, S.; Martinelli, N. G.; Beljonne, D.; Cornil, J.; Genoe, J.; Heremans, P. Unraveling the Mechanism of Molecular Doping in Organic Semiconductors. *Adv. Mater.* **2012**, *24*, 1535−1539.

(48) Gregg, B. A.; Hanna, M. C. Comparing Organic to Inorganic Photovoltaic Cells: Theory, Experiment, and Simulation. *J. Appl. Phys.* **2003**, *93*, 3605−3614.

(49) Madigan, C. F.; Bulović, V. Solid State Solvation in Amorphous Organic Thin Films. *Phys. Rev. Lett.* **2003**, *91*, 247403.

(50) Mamontov, E.; Luo, H.; Dai, S. Proton Dynamics in N,N,N,N-Tetramethylguanidinium Bis(perfluoroethylsulfonyl)imide Protic Ionic Liquid Probed by Quasielastic Neutron Scattering. *J. Phys. Chem. B* **2009**, *113*, 159−169.

(51) Frick, B.; Fetters, L. J. Methyl Group Dynamics in Glassy Polyisoprene: A Neutron Backscattering Investigation. *Macromolecules* **1994**, *27*, 974−980.

(52) Ngai, K. L.; Capaccioli, S.; Paciaroni, A. Change of Caged Dynamics at Tg in Hydrated Proteins: Trend of Mean Squared Displacements after Correcting for the Methyl-group Rotation Contribution. *J. Chem. Phys.* **2013**, *138*, 235102.

(53) Paternó, G.; Cacialli, F.; García-Sakai, V. Structural and Dynamical Characterization of P3HT/PCBM Blends. *Chem. Phys.* **2013**, *427*, 142−146.

(54) Gautam, S.; Liu, T.; Rother, G.; Jalarvo, N.; Mamontov, E.; Welch, S.; Sheets, J.; Droege, M.; Cole, D. R. Dynamics of Propane in Nanoporous Silica Aerogel: A Quasielastic Neutron Scattering Study. *J. Phys. Chem. C* **2015**, *119*, 18188−18195.

(55) Singwi, K. S.; Sjölander, A. Diffusive Motions in Water and Cold Neutron Scattering. *Phys. Rev.* **1960**, *119*, 863−871.

(56) Batchelder, L. S.; Niu, C. H.; Torchia, D. A. Methyl Reorientation in Polycrystalline Amino Acids and Peptides: A Deuteron NMR Spin-lattice Relaxation Study. *J. Am. Chem. Soc.* **1983**, *105*, 2228−2231.

(57) Takegoshi, K.; Imashiro, F.; Terao, T.; Saika, A. 1H and 13C NMR Study on Rotation of Congested Methyl Groups in Methyl Substituted Phenanthrenes, Fluorenes, and Fluorenones. *J. Chem. Phys.* **1984**, *80*, 1089−1094.

(58) Beckmann, P. A.; Cheung, A. M.; Fisch, E. E.; Fusco, F. A.; Herzog, R. E.; Narasimhan, M. Methyl and Tertbutyl Reorientation and Distributions of Activation Energies in Molecular Solids. A Nuclear Spinrelaxation Study in 2,4 and 2,5ditertbutylhydroxybenzene. *J. Chem. Phys.* **1986**, *84*, 1959−1968.

(59) Chahid, A.; Alegria, A.; Colmenero, J. Methyl Group Dynamics in Poly(vinyl methyl ether). A Rotation Rate Distribution Model. *Macromolecules* **1994**, *27*, 3282−3288.

(60) Mukhopadhyay, R.; Alegria, A.; Colmenero, J.; Frick, B. Methyl Group Dynamics in Poly(vinyl acetate):A Neutron Scattering Study. *Macromolecules* **1998**, *31*, 3985−3993.

(61) Moreno, A. J.; Alegría, A.; Colmenero, J.; Frick, B. Methyl Group Dynamics in Poly(methyl methacrylate): From Quantum Tunneling to Classical Hopping. *Macromolecules* **2001**, *34*, 4886−4896.

(62) Duong, D. T.; Wang, C.; Antono, E.; Toney, M. F.; Salleo, A. The Chemical and Structural Origin of Efficient P-type Doping in P3HT. *Org. Electron.* **2013**, *14*, 1330−1336.

(63) Harrelson, T. F.; Cheng, Y. Q.; Li, J.; Jacobs, I. E.; Ramirez-Cuesta, A. J.; Faller, R.; Moulé, A. J. Identifying Atomic Scale Structure in Undoped/Doped Semicrystalline P3HT Using Inelastic Neutron Scattering. *Macromolecules* **2017**, *50*, 2424−2435.

(64) Wiberg, K. B.; Laidig, K. E. Barriers to Rotation Adjacent to Double Bonds. 3. The Carbon-oxygen Barrier in Formic Acid, Methyl Formate, Acetic Acid, and Methyl Acetate. The Origin of Ester and Amide Resonance. *J. Am. Chem. Soc.* **1987**, *109*, 5935−5943.

(65) Heijboer, J.; Baas, J.; van de Graaf, B.; Hoefnagel, M. A Molecular Mechanics Study on Rotational Motions of Side Groups in Poly(methyl methacrylate). *Polymer* **1987**, *28*, 509−513.

(66) Gabrys, B.; Higgins, J. S.; Ma, K. T.; Roots, J. E. Rotational Motion of the Ester Methyl Group in Stereoregular Poly(methyl methacrylate): A Neutron Scattering Study. *Macromolecules* **1984**, *17*, 560−566.

(67) Arrighi, V.; Higgins, J. S.; Burgess, A. N.; Howells, W. S. Rotation of Methyl Side Groups in Polymers: A Fourier Transform Approach to Quasielastic Neutron Scattering. 1. Homopolymers. *Macromolecules* **1995**, *28*, 2745−2753.

(68) Kimura, K.; Kubo, M. Structures of Dimethyl Ether and Methyl Alcohol. *J. Chem. Phys.* **1959**, *30*, 151−158.

(69) Barnes, J. D. Inelastic Neutron Scattering Study of the Rotator Phase Transition in N-nonadecane. *J. Chem. Phys.* **1973**, *58*, 5193−5201.

(70) Fujara, F.; Wefing, S.; Spiess, H. W. Dynamics of Molecular Reorientations: Analogies between Quasielastic Neutron Scattering and Deuteron NMR Spin Alignment. *J. Chem. Phys.* **1986**, *84*, 4579−4584.

(71) Winkler, S.; Amsalem, P.; Frisch, J.; Oehzelt, M.; Heimel, G.; Koch, N. Probing the Energy Levels in Hole-doped Molecular Semiconductors. *Mater. Horiz.* **2015**, *2*, 427−433.

(72) Yim, K. H.; Whiting, G. L.; Murphy, C. E.; Halls, J. J. M.; Burroughes, J. H.; Friend, R. H.; Kim, J.-S. Controlling Electrical Properties of Conjugated Polymers via a Solution-Based p-Type Doping. *Adv. Mater.* **2008**, *20*, 3319−3324.

(73) Tsoi, W. C.; Spencer, S. J.; Yang, L.; Ballantyne, A. M.; Nicholson, P. G.; Turnbull, A.; Shard, A. G.; Murphy, C. E.; Bradley, D. D. C.; Nelson, J.; Kim, J.-S. Effect of Crystallization on the Electronic Energy Levels and Thin Film Morphology of P3HT:PCBM Blends. *Macromolecules* **2011**, *44*, 2944−2952.

(74) Yu, G.; Gao, J.; Hummelen, J. C.; Wudl, F.; Heeger, A. J. Polymer Photovoltaic Cells: Enhanced Efficiencies via a Network of Internal Donor-Acceptor Heterojunctions. *Science* **1995**, *270*, 1789−1791.

(75) Ferguson, A. J.; Kopidakis, N.; Shaheen, S. E.; Rumbles, G. Quenching of Excitons by Holes in Poly(3-hexylthiophene) Films. *J. Phys. Chem. C* **2008**, *112*, 9865−9871.

(76) Watts, B.; Belcher, W. J.; Thomsen, L.; Ade, H.; Dastoor, P. C. A Quantitative Study of PCBM Diffusion during Annealing of P3HT:PCBM Blend Films. *Macromolecules* **2009**, *42*, 8392−8397.

(77) Labram, J. G.; Kirkpatrick, J.; Bradley, D. D. C.; Anthopoulos, T. D. Measurement of the Diffusivity of Fullerenes in Polymers Using Bilayer Organic Field Effect Transistors. *Phys. Rev. B: Condens. Matter Mater. Phys.* **2011**, *84*, 075344.

(78) Labram, J. G.; Kirkpatrick, J.; Bradley, D. D. C.; Anthopoulos, T. D. Impact of Fullerene Molecular Weight on P3HT:PCBM Microstructure Studied Using Organic Thin-Film Transistors. *Adv. Energy Mater.* **2011**, *1*, 1176−1183.

(79) Berriman, G. A.; Holdsworth, J. L.; Zhou, X.; Belcher, W. J.; Dastoor, P. C. Molecular versus Crystallite PCBM Diffusion in P3HT: PCBM Blends. *AIP Adv.* **2015**, *5*, 097220.